Journal of The Korean Astronomical Society
45: 157 ∼ 166, 2012 December

http://dx.doi.org/10.5303/JKAS.2012.45.6.157
ISSN:1225-4614
http://jkas.kas.org

SMA OBSERVATIONS OF THE HOT CORES OF DR21(OH)

Y. C. Minh[1], H.-R. Chen[2], Y.-N. Su[3], and S.-Y. Liu[3]
[1] Korea Astronomy and Space Science Institute, Daedeok-daero 776, Yuseong-gu, Daejeon 305-348, Korea
E-Mail : minh@kasi.re.kr
[2] Institute of Astronomy & Department of Physics, National Tsing Hua University, Hsinchu 30013, Taiwan
E-Mail : hrchen@nthu.edu.tw
[3] Academia Sinica, Institute of Astronomy and Astrophysics, P. O. Box 23-141, Taipei 106, Taiwan
E-Mail : ynsu@asiaa.sinica.edu.tw, syliu@asiaa.sinica.edu.tw
(Received August 17, 2012; Revised September 11, 2012; Accepted November 14, 2012)

ABSTRACT

Using the Submillimeter Array (SMA), we identified two bright hot subcores, MM1a and MM1b (size $\sim 1''$ and mass ~ 0.5 $M_\odot$) separated by about $1.6''$, in the 230 GHz continuum emission toward the massive star-forming region DR21(OH). Both display typical hot core characteristics but have slightly different chemical properties. For example, highly saturated species show stronger emission toward MM1a and seem to be evaporating directly from the grain mantles. In contrast, simple sulfur-bearing species have brighter emission at MM1b. These features indicate that MM1a is at an earlier stage than MM1b, and the small-scale chemical differences between these two cores may result from the age difference of the order of 10^4 years.

Key words : ISM: abundances — molecules — : individual(DR21(OH)) — stars: formation

1. INTRODUCTION

Hot cores found in the vicinity (≤ 0.1 pc) of newly formed massive stars represent one of the earliest stages in the evolution of massive stars. They are believed to occur almost immediately after the formation of a protostar but before the protostar has sufficient power to ionize all of the surrounding gas (Kurtz et al. 2000). They are small ($10^{-2} - 10^{-1}$ pc), dense ($\geq 10^7$ H_2 cm^{-3}), and relatively warm (≥ 100 K) gas cores, believed to be the remnants of the cloud that collapsed in the process of forming the massive star (e.g., Viti & Williams 1999; Kurtz et al. 2000). Hot cores have rich chemistry, especially in saturated molecules that are believed to arise from the evaporation of ice mantles frozen-out onto the dust grains during the cloud collapse. Various molecular lines detected in the hot cores provide unique tools for understanding the very early phase of star-forming processes. Recent technological progress in bolometer arrays and (sub-)millimeter interferometers have enabled high sensitivity and high spatial resolution observations to be used to study the details of deeply embedded, complicated, and crowded massive star-forming cores. Here we report the results of observations on hot cores in the massive star-forming region DR21(OH) using the Submillimeter Array (SMA).

DR21(OH) is one of the prominent massive star-forming cores in the Cygnus X region, one of the richest molecular and HII complexes located at a distance of 1.4 kpc (Rygl et al. 2012; Schneider et al. 2006; Motte et al. 2007). The molecular complex is massive (4×10^6 $M_\odot$), over ∼100 pc in diameter, and contains several OB associations, including one of the largest in our Galaxy (Cyg OB2). DR21(OH) is associated with masers of OH (Norris et al. 1982; Argon et al. 2000), H_2O (Genzel & Downes 1977), and CH_3OH (Batrla & Menten 1988; Plambeck & Menten 1990; Kogan & Slysh 1998; Kurtz et al. 2004; Araya et al. 2009; Fish et al. 2011), which is indicative of ongoing star formation activity. This source consists of several dense clumps (Mass $\sim 10^3$ $M_\odot$ and n(H_2) $\sim 10^6$ cm^{-3}) separated by $30''$ to $50''$ (Mangum et al. 1991), and is likely to harbor multiple sources at a very early stage of star formation. Woody et al. (1989) identified two bright compact cores at 1.4mm, MM1 and MM2, separated by about $8''$ from each other in the northeast-southwest direction. MM1 shows a much stronger continuum emission than MM2 at millimeter wavelengths (Woody et al. 1989; Liechti & Walmsley 1997; Lai et al. 2003). Subsequent interferometric observations have further resolved MM1 and MM2 into several subcores (Araya et al. 2009; Zapata et al. 2012).

We conducted SMA observations toward the MM1 and MM2 region of DR21(OH) at 230 GHz and 340 GHz. In this paper, we summarize the observations in Section 2 and the results in Section 3 for the continuum and molecular line properties. The chemistry of the hot cores is discussed in Section 4, and conclusions are presented in Section 5.

Corresponding Author: Y. C. Minh

2. OBSERVATIONS

DR21(OH) was observed with the Submillimeter Array*(SMA: Ho et al. 2004) in 2006 May 23th at 230 GHz and 2006 August 23th at 340 GHz. Eight antennas of the array were used in an extended configuration for the 230 GHz observations, which provided a synthesized beam of $\sim 1.0'' \times 0.9''$ (PA $= -74°$) by natural weighting. For the 340 GHz observations, seven antennas were used instead due to a technical problem; this resulted in a synthesized beam of $\sim 2.2'' \times 1.9''$ (PA $= -32°$). The primary field of view was $56''$ and $38''$ at 230 and 340 GHz, respectively. Heterodyne SIS receivers were used and system temperatures ranged between 120 and 240 K for the different antennas. During the observations, the zenith atmospheric opacities were ~ 0.1 and 0.2 at 230 and 340 GHz, respectively. The RF bandpass has been calibrated on the quasar 3C454.3, and Neptune was used for flux calibration. The phase reference of the array was set to the position (R. A., decl.)$_{J2000}$ = ($20^h38^m36^s.397$, $40°37'27''.99$). We integrated the continuum emission over the line-free channels from both upper and lower sidebands, resulting in a total bandwidth of ∼3.8 GHz and an RMS noise level of 1 mJy/beam and 5 mJy/beam for 230 GHz and 340 GHz continuum observations, respectively. The instrumental spectral resolution was 0.8125 MHz, with resulting RMS noise levels of about 30 and 40 mJy/beam per channel, at 230 and 340 GHz, respectively. The continuum was subtracted from the line visibilities prior to imaging. The data reduction and calibration were conducted under MIR/IDL†, and the imaging and data analysis were processed under MIRIAD.

3. RESULTS

3.1 Continuum Emission

Fig. 1 shows the continuum emission distribution at 230 GHz overlaid on the 340 GHz emission. In our high spatial resolution (∼1″) observation, we found several sub-cores in both MM1 and MM2, in agreement with the previous report by Zapata et al. (2012), but we labeled the three bright sub-cores only associated with MM1 as MM1a, b, and c (Fig. 1). Araya et al. (2009) found a cluster of centimeter continuum sources toward the center of MM1b. The MM1-NW and MM1-SE continuum sources were interpreted as a single radio jet with a spectral index of about 0.8, indicating thermal free-free emission. They also reported an H_2O maser source (from P. Palmer & M. Goss, in preparation) between MM1-NW and MM1-SE, at the center of MM1b. However, no centimeter continuum and no

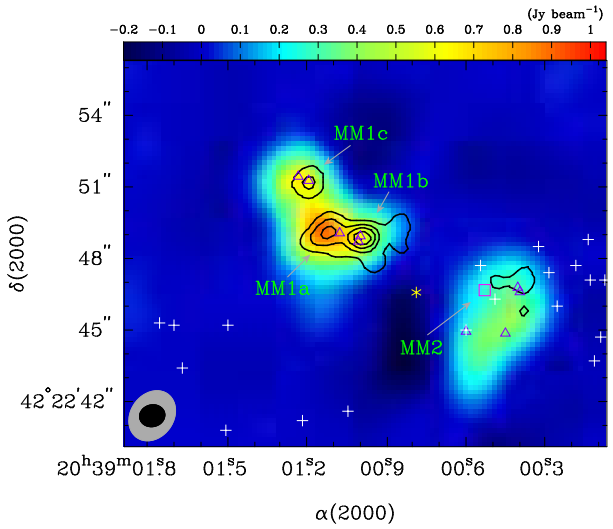

Fig. 1.— Continuum distributions at 230 GHz (contours) and 340 GHz (false color). Scales are inserted for the 340 GHz continuum emission. Contours of the 230 GHz emission show the 20% levels of the peak intensity (0.13 Jy beam^{-1}). The beams are shown in the lower left as ellipses (grey for 340 GHz and black for 230 GHz). The asterisk is the H_2O maser position (Genzel & Downes 1977) and the crosses are methanol masers (Araya et al. 2009). The MM2 position (Woody et al. 1989) is shown as a box (magenta). Triangles (purple) are the SMA sources listed by Zapata et al. (2012).

maser sources were detected toward MM1a. The position of MM1c coincides with the north lobe center of the H_2CS bipolar outflow, as reported by Minh et al. (2011), which is roughly aligned north-south from MM1a. Since the molecular line emissions of the hot core species have not been detected towards MM1c, this continuum peak is believed to mainly result from heated dust from the interaction with outflows from MM1a (Minh et al. 2011).

Several sub-cores were found toward MM2, but with much weaker continuum intensities compared to the bright MM1 sub-cores (Fig. 1). We also have not detected any appreciable emission from the observed molecular lines toward MM2 as shown in Fig. 2, suggesting that this core does not have apparent hot cores at present. But several authors have found methanol masers largely scattered in the east-west direction, as summarized in Section 1, that are associated with MM2 ("crosses" in Fig. 1). Araya et al. (2009) reported a weak radio continuum source (R1) and H_2O masers (P. Palmer & M. Goss, in preparation) associated with MM2. It is not yet certain, however, whether some subcores in MM2 are actually powering these masers and will eventually appear as hot cores. In this paper, we focus on the hot core features of MM1a and MM1b, where molecular emissions are found to be strongly concentrated.

The millimeter continuum emission of MM1 is thought

*The Submillimeter Array is a joint project between the Smithsonian Astrophysical Observatory and the Academia Sinica Institute of Astronomy and Astrophysics and is funded by the Smithsonian Institution and the Academia Sinica.

†http://cfa-www.harvard.edu/∼cqi/mircook.html

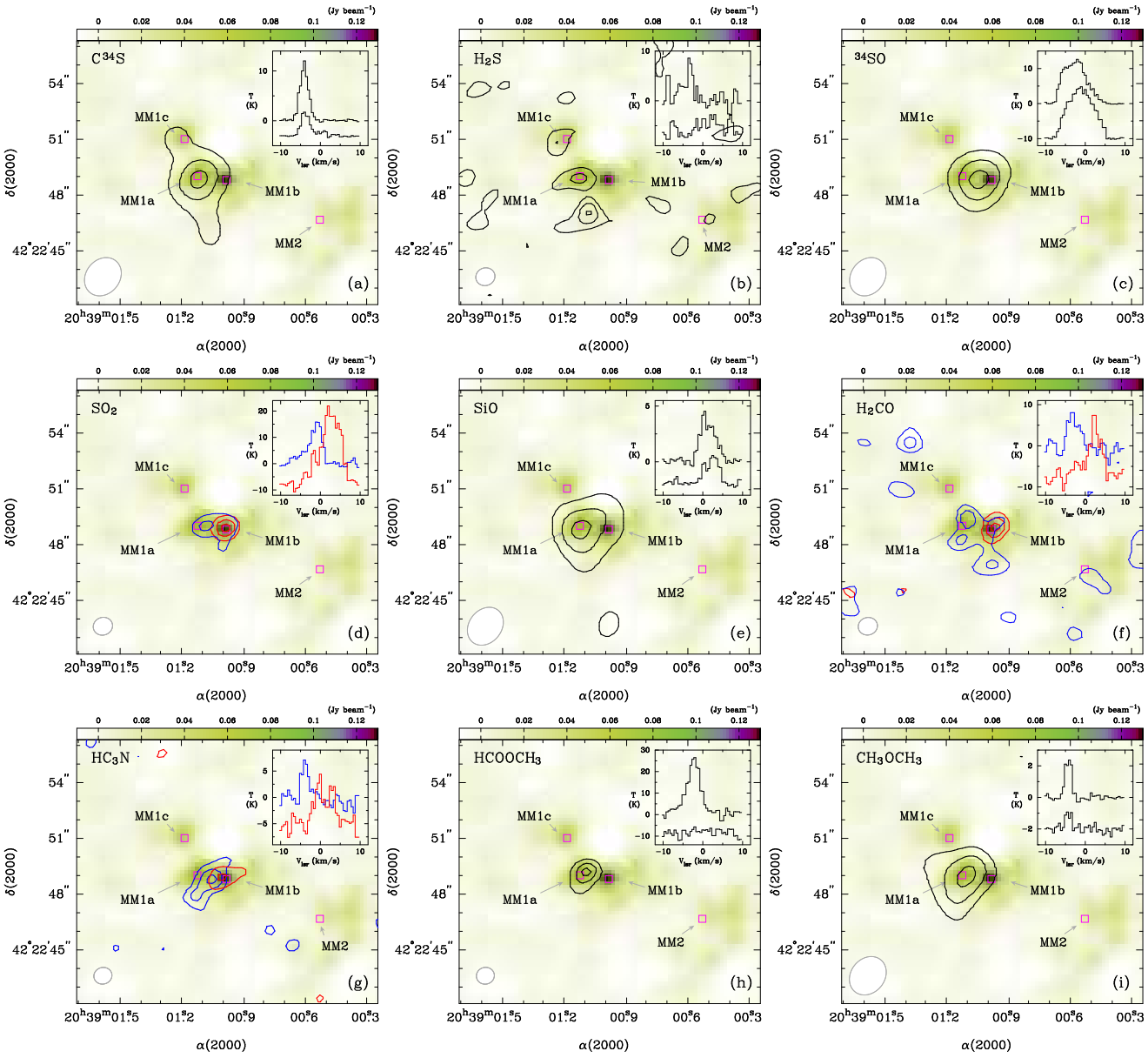

Fig. 2.— Integrated intensity distributions of the observed transitions used to derive abundances in Table 3. The background is the 230 GHz continuum of Fig. 1 (scales inserted). The inset in the upper right shows sample spectra taken toward MM1a (upper spectrum) and MM1b (lower spectrum). The beam of the observed transition is shown in the bottom left side. All contours are 30%, 60%, and 90% of the peak emission. The red and blue contours in (d), (f), and (g) are the results for different velocity ranges ($v = -8 \sim 0$ for blue and $0 \sim 8$ km s^{-1} for red) and their spectra are shown in the inset of each figure. (a) $C^{34}S$ $(7-6)$; (b) H_2S $(2_{2,0}-2_{1,1})$; (c) ^{34}SO (8_8-7_7); (d) SO_2 $(22_{2,20}-22_{1,21})$; (e) SiO $(8-7)$; (f) H_2CO $(3_{2,2}-2_{2,1})$; (g) HC_3N $(25-24)$; (h) $HCOOCH_3$ $(20_{2,19}-19_{2,18}$ A); and (i) CH_3OCH_3 $(21_{2,19}-20_{3,18}$ EE).

to trace mainly warm dust heated by the embedded YSOs. However, the free-free continuum sources found toward MM1b at centimeter wavelengths (Araya et al. 2009) would contribute about 20% (about 42.2 mJy from MM1-NW and MM1-SE) of the observed 230 GHz flux using the suggested spectral index of 0.82. From the expected 230 GHz flux from dust, we derive the total mass of the MM1 sub-cores using the method summarized by Hildebrand (1983). This method assumes that gas and dust are coupled together; see Minh et al. (2010) for details. Dust temperatures exert the largest influence on the derivation of the physical parameters of these sub-cores from the continuum emission.

Therefore, we applied the ±50% error range for the expected dust temperature of $T_d = 200$ K for MM1a and MM1b. This value is not only the canonical value

Table 1.
Parameters of the identified continuum cores at 230 GHz.

Source	Position[a] ($''$, $''$)	Peak[b] (mJy/beam)	Total Flux[b] (mJy)	Size[b] ($'' \times ''$)	P.A.[b] ($^\circ$)	$T_{\rm dust}$ (K)	$M_{\rm core}$ ($M_\odot$)	$N_{\rm H_2}$ ($\rm cm^{-2}$)	$n_{\rm H_2}$ ($\rm cm^{-3}$)
MM1a	(0, 0)	86 ±15	157 ±20	(1.6 ±0.3)×(1.1 ±0.2)	−46 ±19	200 ∓ 100	$0.23\ ^{+0.25}_{-0.08}$	$1.3\ ^{+1.4}_{-0.5} \times 10^{23}$	$3.5\ ^{+3.7}_{-1.2} \times 10^{6}$
MM1b	(−1.6, −0.2)	112 ±10	293 ±21	(1.9 ±0.2)×(1.4 ±0.3)	−83 ±98	200 ∓ 100	$0.43\ ^{+0.46}_{-0.15}$	$1.1\ ^{+1.2}_{-0.4} \times 10^{23}$	$2.0\ ^{+2.1}_{-0.7} \times 10^{6}$
MM1c	(0.7, 2.2)	56 ±9	168 ±22	(2.0 ±0.4)×(1.5 ±0.3)	89 ±22	100 ∓ 50	$0.51\ ^{+0.57}_{-0.18}$	$1.0\ ^{+1.1}_{-0.6} \times 10^{23}$	$1.6\ ^{+1.8}_{-0.5} \times 10^{6}$

[a]Offset from the MM1a position: $(\alpha,\ \delta)_{2000} = (20^h39^m01.125^s,\ 42^\circ22'49.01'')$
[b]Derived by gaussian fit using `'imfit'` in the MIRIAD software package.

Table 2.
Molecular line parameters observed towards MM1a and MM1b

Molecule	Transition	Freq.[a] (GHz)	$T_{\rm peak}$[b,c] (K)	$v_{\rm peak}$[b,c] (km s^{-1})	$\Delta v_{\rm HP}$[b,c] (km s^{-1})	Flux[c] (K km s^{-1})	RMS[d] (K)
$C^{34}S$	$7-6$	337.3965	10.9/4.7	−4.1/−3.8	2.5/2.6	29.9/14.4	0.21
H_2S	$2_{2,0}-2_{1,1}$	216.7104	6.0/ –	−3.6/ –	3.7/ –	21.2/ –	1.53
^{33}SO	$N,J=8,7-7,6$	337.1997	2.7/1.5	−1.7/−0.6	3.9/6.9	11.3/10.6	0.23
^{34}SO	$N,J=8,8-7,7$	337.5802	12.4/14.4	−2.7/−1.2	6.8/7.6	87.4/115.7	0.40
SO_2	$22_{2,20}-22_{1,21}$	216.6433	14.9/26.9	−1.2/2.7	2.4/5.9	63.7/188.4	1.78
SO_2	$18_{4,14}-18_{3,15}$	338.3060	10.4/15.1	−1.1/0.4	11.9/7.4	72.2/117.9	0.25
SO_2	$24_{2,22}-23_{3,21}$	348.3878	6.7/9.5	−0.6/1.3	6.9/7.1	10.6/71.6	0.26
$^{34}SO_2$	$12_{3,9}-12_{2,10}$	227.0319	13.0/ –	0.9/ –	2.4/ –	45.8/ –	1.54
$^{34}SO_2$	$19_{4,16}-19_{3,17}$	348.1175	0.7/1.9	0.5/0.7	4.0/6.4	3.7/9.5	0.24
SiO	$5-4$	217.1050	6.9/ –	0.5/ –	4.3/ –	33.3/ –	1.67
SiO	$8-7$	347.3308	3.8/2.3	1.2/2.3	4.4/4.1	18.1/10.4	0.19
H_2CO	$9_{1,8}-9_{1,9}$	216.5687	10.8/ –	−3.7/ –	3.1/ –	35.3/ –	1.53
H_2CO	$3_{0,3}-2_{0,2}$	218.2222	– /24.9	– /2.8	– /3.5	– /110.6	1.66
H_2CO	$3_{2,2}-2_{2,1}$	218.4756	8.4/12.2	−2.9/2.4	3.2/3.5	25.6/49.1	1.52
HC_3N	$24-23$	218.3247	17.4/6.6	−3.8/1.9	2.2/3.7	39.4/24.4	1.50
HC_3N	$25-24$	227.4189	7.3/7.0	−3.8/1.0	2.1/6.3	15.7/44.3	1.47
HCOOH	$15_{5,11}-14_{5,10}$[e]	337.7851	6.5/2.6	−6.1/−6.3	2.2/2.6	15.5/5.5	0.23
$HCOOCH_3$	$20_{1,20}-19_{1,19}$ E[f]	216.9648	17.2/3.8	−5.3/−1.2	5.3/7.4	67.9/15.8	1.50
$HCOOCH_3$	$20_{2,19}-19_{2,18}$ A	226.7188	15.7/ –	−3.5/ –	1.5/ –	20.7/ –	1.61
$HCOOCH_3$	$21_{1,21}-20_{1,20}$ A[g]	227.5628	24.5/ –	−2.3/ –	3.7/ –	88.4/ –	1.62
$HCOOCH_3$	$26_{6,20}-25_{6,19}$ A	336.9182	2.9/ –	−4.0/ –	1.6/ –	6.0/ –	0.17
$HCOOCH_3$	$27_{8,19}-26_{8,18}$ A	338.3558	2.0/ –	−4.3/ –	1.4/ –	3.1/ –	0.22
CH_3OCH_3	$21_{2,19}-20_{3,18}$ EE[h]	337.4210	2.6/1.0	−4.3/−4.3	1.8/1.6	4.9/1.9	0.24
CH_3OCH_3	$7_{4,4}-6_{3,3}$ EE[i]	337.7224	3.5/0.7	−4.3/−4.5	1.9/1.9	7.8/2.4	0.31
CH_3OCH_3	$7_{4,4}-6_{3,3}$ EA[j]	337.7319	4.4/1.0	−3.6/−3.3	3.0/3.4	13.2/4.9	0.23

[a]From Lovas et al. (2009). [b]Gaussian fit values. [c]Left ones and right ones of the slashes are for MM1a and MM1b, respectively. [d]1σ.
[e]Overlapped with the HCOOH $15_{5,10}-14_{5,9}$ (337.7878 GHz) and CH_3OCH_3 $7_{4,3}-6_{3,4}$ AA (337.7872 GHz) and EE (337.7879 GHz) transitions. [f]Overlapped with the $HCOOCH_3$ $20_{1,20}-19_{1,19}$ A (216.9659 GHz) and $20_{0,20}-19_{0,19}$ E (216.9662 GHz) and A (216.9674 GHz) transitions. [g]Overlapped with the $HCOOCH_3$ $21_{0,21}-20_{0,20}$ A (227.5628 GHz), $21_{0,21}-20_{0,20}$ E (227.5617 GHz), and $21_{1,21}-20_{1,20}$ E (227.5609 GHz) transitions. [h]Overlapped with the CH_3OCH_3 $21_{2,19}-20_{3,18}$ AA (337.4205 GHz) and AE+EA (337.4216 GHz) transitions. [i]Overlapped with the CH_3OCH_3 $7_{4,4}-6_{3,3}$ AE (337.7230 GHz) transition. [j]Overlapped with the CH_3OCH_3 $7_{4,3}-6_{3,3}$ EE (337.7322 GHz) and $7_{4,4}-6_{3,3}$ AA (337.7307 GHz) transitions.

for general hot cores but also the expected temperature from multiline methanol observations toward these cores (see Section 3.3 for observed methanol results). Although T_d = 100 K for MM1c associated with the outflow component (Minh et al. 2011) is somewhat arbitrary, the applied error range is believed to account for the expected uncertainty.

Further discussions on other parameters used within the equations may be found in Section 3.1 of Minh et al. (2010). Table 1 summarizes the continuum parameters derived for the MM1 cores. These cores have masses of $\sim$0.5 $M_\odot$, $N_{H_2} \sim 10^{24}$ cm^{-2}, with volume densities of about $10^7 - 10^8$ cm^{-3} assuming spherical shapes. Since these masses appear to be less than those of typical hot cores, we will refer to them as hot subcores. The MM1a and MM1b cores are separated by only 1.6″ which corresponds to $\sim$ 2200 AU at a 1.4 kpc distance; this may indicate a binary or a multiple system.

3.2 Molecular Line Emission Distributions

Various molecular lines have been detected toward MM1 of DR21(OH) within our total $\sim$8 GHz bandwidth observed at the 230 GHz and 340 GHz wavelengths. In addition to simple sulfur- and oxygen-bearing species, highly saturated species characterizing the hot core also appear to be abundant. Significant parts in the observed wavelength band, however, appear to be highly confused by overlaps of the emission lines. Table 2 lists the observed parameters of molecular lines that are selected from the detected lines toward MM1a and MM1b based on a lack of confusion with nearby lines. A few tens of methanol transitions have also been detected toward this source, which will be discussed in the next section (Section 3.3).

The observed molecular emissions are strongly concentrated toward MM1a and b, as well as the 230 GHz continuum emission. These emissions show extended features with various morphologies, which may suggest the existence of other subcores other than MM1a and b. Here we discuss on the beam-averaged features in these two hot subcores MM1a and b. There exists a difference in the molecular emission distributions between these two cores depending on the species. Roughly speaking, one group of emission lines peaks toward MM1a, and a second group peaks toward MM1b. The first group includes highly saturated molecules, such as CH_3OH, $HCOOCH_3$ and CH_3OCH_3. In contrast, the second group contains sulfur-containing species such as SO and SO_2. MM1b is about 50% brighter in the 230 GHz continuum than MM1a, and is also associated with OH masers and probably a driving source for H_2O masers (Argon et al. 2000; Genzel & Downes 1977).

Fig. 2 shows the velocity integrated intensity maps of the lines, which are used to derive the abundances listed in Table 2. The $C^{34}S$ line intensity peaks toward MM1a with an extended emission feature roughly along the north-south direction (Fig. 2a). This extended feature is shared with H_2CS lines as reported by Minh et al. (2011), and is also shared with a few CH_3OH lines (see Section 3.3). We believe that this feature is related to the outflow associated with MM1a (Minh et al. 2011). The H_2S is relatively weak but shows extended emission along the outflow positions north and south of MM1a. This feature may suggest that H_2S is not a major ice mantle component, but forms in the interacting region between the outflow and the ambient gas. Emissions from sulfur-bearing species in general are concentrated strongly toward MM1b, which is probably a result from the higher excitation temperatures in MM1b. The 216 GHz transition of SO_2 (Fig. 2d), with a beam size of $\sim 1''$, clearly distinguishes the emissions from MM1a and b, since there is a velocity difference between these two sources. Both SiO $5-4$ and $8-7$ emissions appear to be centered roughly at MM1a, but interestingly their lines show a velocity of MM1b although the $5-4$ line show more scatter all over the region. As an unambiguous shock tracer, the SiO emission is probably associated with the outflow from MM1a that was observed with the H_2CS emission (Minh et al. 2011). Three lines from H_2CO have been detected toward both MM1a and b. The high energy level transitions show a stronger emission at MM1a and lower energy level transitions at MM1b. The HC_3N lines show brighter emissions at MM1b. The highly saturated species, CH_3OH, $HCOOCH_3$ and CH_3OCH_3, are clearly concentrated toward MM1a, which suggests that MM1a is the later hot subcore. Although there are uncertainties in distinguishing MM1a and b, especially for 340 GHz transitions of about 2″ spatial resolutions, there are clear differences between MM1a and b in molecular emissions which probably resulted from the different chemical properties of these cores.

3.3 Methanol Emission Lines

Many methanol lines have been detected in this observation including torsionally excited lines. Table 3 lists the observed parameters for the selected lines which have been identified without ambiguity. In general, methanol line emissions show strong concentration towards MM1, as shown in Fig. 3. Some transitions (about 3 transitions of $E_u \leq 50$ K, as indicated in the note of Table 3) have extended emissions near MM2 and southern maser emission regions. The sample map is shown in Fig. 3a for the $7_{-1,7} - 6_{-1,6}$ E transition. These features seem to indicate that there exist some cloud activities making the ice component evaporate from the dust mantles. It is probable these methanol emissions show that the clouds are collapsing in this region without yet developing hot cores. Among these three lines, two transitions show extended component along the north-south direction of MM1 (including MM1c), which is similar to the H_2CS outflow feature discussed by Minh et al. (2011). This extended emission may arise via the same mechanism as for the H_2CS emission, namely, the evaporation of dust ice mantles in the turbulent gas caused by interaction of outflows with ambient gas.

Table 3.
CH_3OH line parameters observed towards MM1a and MM1b

Transition	Freq. (GHz)	T_{peak} [a,b] (K)	v_{peak} [b,c] (km s^{-1})	Δv_{HP} [a,b] (km s^{-1})	Flux[b] (K km s^{-1})	RMS[c] (K)	Note
$5_{1,4} - 4_{2,2}$ E	216.9456	25.6/7.7	−3.6/2.2	2.6/4.9	58.5/35.5	1.85	
$6_{1,5} - 7_{2,6}$ A$^-$ v_t=1	217.2992	14.9/3.0	−3.5/4.5	3.4/2.7	48.1/16.2	1.84	
$20_{1,19} - 20_{0,20}$ E	217.8864	12.0/5.0	−3.7/3.3	2.9/3.7	24.9/16.4	1.92	
$4_{2,2} - 3_{1,2}$ E	218.4401	31.8/21.7	−3.4/2.2	3.1/3.9	86.7/88.5	1.97	d
$12_{1,11} - 12_{0,12}$ A^{-+}	336.8652	22.2/11.0	−3.4/1.6	4.2/5.5	94.8/53.2	0.36	
$3_{3,0} - 4_{2,2}$ E	337.1359	9.5/1.0	−3.8/3.9	2.5/4.3	25.1/3.7	0.25	
$7_{1,7} - 6_{1,6}$ A^{++} v_t=1	337.2975	9.1/1.8	−3.6/1.3	3.8/3.5	34.4/3.8	0.34	
$7_{-6,2} - 6_{-6,1}$ E v_t=1	337.4905	2.9/ –	−3.6/ –	1.6/ –	5.0/ –	0.27	
$7_{3,5} - 6_{3,4}$ E v_t=1	337.5191	6.3/1.3	−3.9/2.1	2.7/2.9	17.5/4.2	0.39	
$7_{2,5} - 6_{2,4}$ A^{++} v_t=1	337.6258	11.4/1.2	−3.7/4.0	2.5/0.5	34.8/4.4	0.28	
$7_{2,6} - 6_{2,5}$ E v_t=1	337.6712	6.9/0.5	−3.8/4.9	2.0/2.3	16.8/2.8	0.24	
$7_{-1,6} - 6_{-1,5}$ E v_t=1	337.7075	5.5/0.7	−4.0/4.5	2.9/5.1	19.7/3.1	0.34	
$7_{0,7} - 6_{0,6}$ A^{++} v_t=1	337.7488	6.9/1.0	−4.0/1.3	2.8/4.1	18.1/3.3	0.35	
$7_{1,6} - 6_{1,5}$ A^{--} v_t=1	337.9694	9.7/2.1	−3.8/2.9	2.7/1.3	27.1/3.8	0.29	
$7_{0,7} - 6_{0,6}$ E	338.1245	16.3/7.7	−3.9/2.1	3.7/3.7	57.7/31.5	0.43	d,e
$7_{-1,7} - 6_{-1,6}$ E	338.3446	13.8/8.4	−3.8/2.3	3.4/3.6	52.5/25.1	0.35	d,e
$7_{-6,1} - 6_{-6,0}$ E	338.4310	9.0/1.6	−3.9/2.0	2.8/2.6	27.5/4.4	0.31	
$7_{-5,2} - 6_{-5,1}$ E	338.4565	13.2/1.9	−3.9/1.5	3.1/3.9	47.2/7.6	0.31	
$7_{5,3} - 6_{5,2}$ E	338.4752	12.2/5.0	−3.7/2.1	3.4/2.3	48.0/14.8	0.36	
$7_{-3,5} - 6_{-3,4}$ E	338.5599	17.9/5.4	−3.7/1.6	3.9/4.1	70.3/22.3	0.32	
$7_{3,4} - 6_{3,3}$ E	338.5832	19.4/5.6	−3.8/0.3	3.6/6.6	74.7/23.3	0.31	
$7_{2,5} - 6_{2,4}$ A$^+$	338.6398	18.8/6.3	−3.6/2.2	3.8/5.1	60.2/31.9	0.27	

[a]Gaussian fit values. [b]Left ones and right ones of the slashes are for MM1a and MM1b, respectively. [c]1σ. [d]Weak extended emission features exist near MM2 and southern maser sources. [e]Extended features around MM1c, similar to those of the H_2CS outflow explained in Minh et al. (2011).

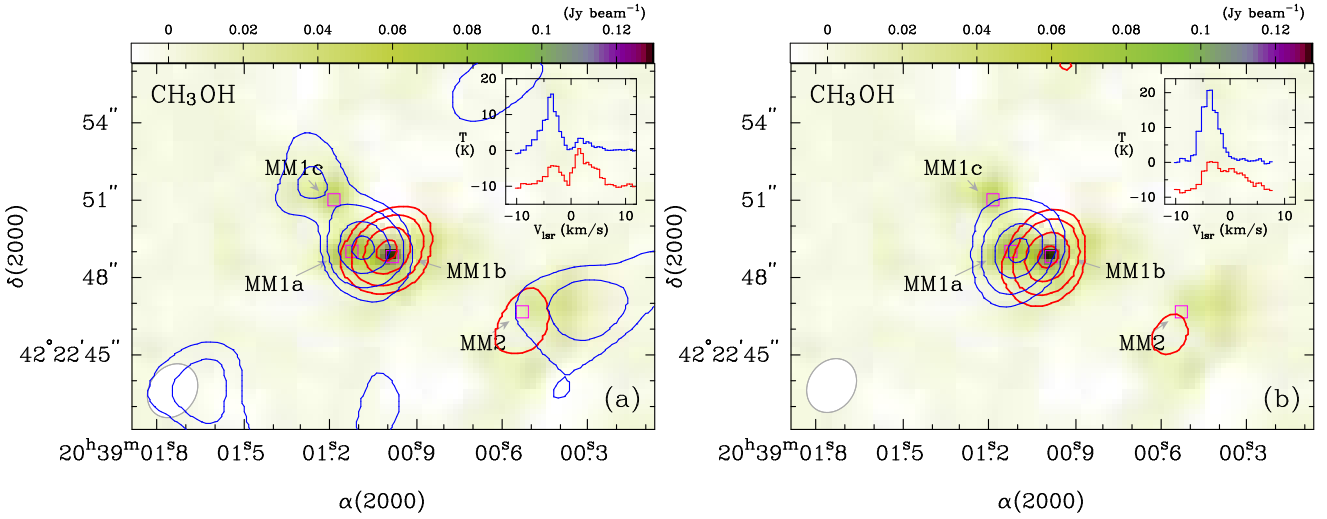

Fig. 3.— Integrated intensity map of CH_3OH (a) for the $7_{-1,7} - 6_{-1,6}$ E line; (b) for the $7_{3,4} - 6_{3,3}$ E line. The lowest contour level is the 15% of the peak intensity to show the extended component around the MM1c, and then the 30% levels of the peak intensity as for Fig. 2. Other features are same as in the caption of Fig. 2.

Most of other methanol lines appear to be highly concentrated in MM1 core, and a sample map is shown in Fig. 3b for the $7_{3,4} - 6_{3,3}$ E transition. In this paper, we focus on the properties of the hot cores in MM1 and differences between the subcore MM1a and b. As shown in the insets of Fig. 3, the spectra show two velocity components, at about −4 and 1 km s^{-1}. This velocity difference is easily distinguishable in the spectra, and those two velocities correspond to MM1a and b, respectively. Fig. 4 shows the rotational diagrams of the observed methanol lines in Table 3, which clearly indicate the existence of at least two components at temperatures of about 20 K and 200 K. We may then expect that the 200 K component represents the hot core and the 20 K component is the envelope surrounding the hot core.

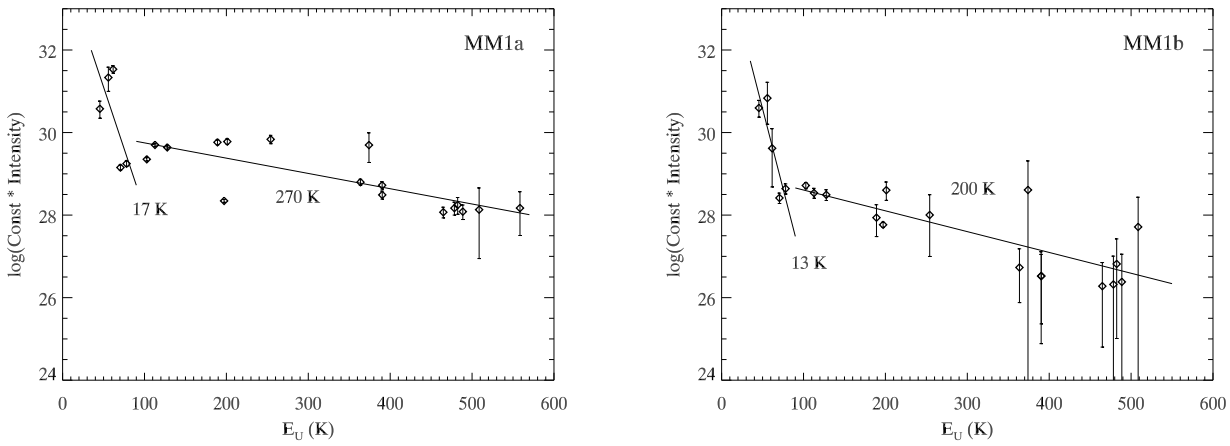

Fig. 4.— Rotational diagrams of the observed CH_3OH lines in Table 3. Error bars are for the observed 3σ uncertainties. Derived rotational temperatures are indicated.

3.4 Abundances of the Observed Molecules

We derive beam-averaged abundances of the observed species towards MM1a and b. Firstly, methanol abundances were derived using the rotational diagrams (Fig. 4) for the 200 K and 20 K components separately, which correspond to the hot core and the envelope components, respectively. Since hot cores are embedded in the center of dense clouds, it will be difficult to define their parameters unambiguously. The source parameters in Table 1 were derived from the dust continuum emission which is sensitive to high temperature component, and we think that those values represent the 200 K hot core component where gas and dust are expected to be well coupled.

It is also difficult to determine whether the observed molecule exists mainly in the hot core or in the envelope which will be crucial in deriving its abundance. Higher spatial resolution observations will be necessary to clarify this issue. The saturated species, $HCOOCH_3$ and CH_3OCH_3, which seem to coexist with CH_3OH, were regarded as hot core components at a rotational temperature of 200 K in deriving their abundances. Since SO and SO_2 show a strong concentration towards MM1b which probably trace high temperature gas associated with embedded YSOs (e.g., Minh et al. 2010), we also assumed T_{rot} = 200 K for these species. The HC_3N emission appears to be concentrated towards MM1b and the region between MM1a and b as shown in Fig. 2g ($E_u \approx 140$ K). HC_3N also exists in the high temperature gas associated with YSOs or in the interacting regions between MM1a and b, suggesting that T_{rot} = 200 K for this molecule as well. Other species, H_2S, SiO, and H_2CO, are expected to exist partly in the hot cores but also partly in the envelope gas, and so we arbitrarily set T_{rot} = 100 K for these species. On the other hand, CS is thought to exist mainly in the envelop at a temperature T_{rot} = 20 K.

Results are listed in Table 4. The second column is the rotational temperature used to derive their abundances. The 50% uncertainty of T_{rot} results in $\lesssim$ 30 % uncertainty in abundances, except for CS (about 10 times higher abundance if T_{rot} = 10 K). The uncertainties from the observed RMS values (the last column of Table 2) are relatively small and less than those from the T_{rot} ranges. Since these are beam-averaged abundances and our beam sizes are different for the transitions observed at 230 GHz ($\sim 1''$) and 340 GHz ($\sim 2''$), there should be additional uncertainties. However, these uncertainties are expected to be small because the observed lines extend well out of the one-beam sizes. We may thus expect that the overall uncertainties of the derived abundances are less than a factor of two.

Table 4 also includes the fractional abundances of the observed species relative to the total H_2 abundance in Table 1. In general, the total H_2 abundance is difficult to estimate accurately, which would lead to further uncertainty if the relative abundances with H_2 are referenced. In this source, however, the H_2 abundance was derived from the warm dust emission which is certainly associated with the hot core and most of the observed species show a strong concentration towards the hot subcores MM1a or MM1b. Therefore, we expect that the fractional abundances relative to H_2 in Table 4 could provide a good constraint in discussing hot core properties. We also include the relative abundances compared to the derived SO abundance for comparison. The SO abundance seems to be somewhat consistent during the hot core phase but subsequently it disappears quickly (Minh et al. 2010). Therefore, we think that the comparison of abundances with SO could be a good reference in discussing the hot core chemistry.

Table 4.
Abundances of the observed species

Molecule	T_{rot} (K)	MM1a N_{column}[a] (cm^{-2})	MM1a [x]/[H_2] [a]	MM1a [x]/[SO]	MM1b N_{column}[a] (cm^{-2})	MM1b [x]/[H_2] [a]	MM1b [x]/[SO]	Note
CS	20	5.3(15)	-	-	2.6(15)	-	-	c,d
H_2S	100	1.8(15)	1(-8)	0.1	≤1.5(15)	≤1(-8)	≤0.1	e
SO	200	1.6(16)	1(-7)	1	2.1(16)	2(-7)	1	f,d
SO_2	200	1.6(16)	1(-7)	1	4.6(16)	4(-7)	2	g
SiO	100	3.8(14)	3(-9)	0.02	2.2(13)	2(-10)	0.001	h
H_2CO	100	2.4(15)	2(-8)	0.2	4.5(15)	4(-8)	0.2	i
HC_3N	200	6.2(13)	5(-10)	0.004	1.7(14)	2(-9)	0.01	j
$HCOOCH_3$	200	1.7(16)	1(-7)	1	≤6.1(15)	≤6(-8)	≤0.3	k
CH_3OCH_3	200	4.2(15)	3(-8)	0.3	1.6(15)	1(-8)	0.1	l
CH_3OH (core)	200[b]	3.6(15)	3(-8)	0.2	7.9(14)	7(-9)	0.04	m
(env)	20[b]	1.6(16)	-	-	3.6(15)	-	-	m

[a] $x(y)$ means $x \times 10^y$. [b] Rotational diagram results (Fig. 4) were applied. [c] From the $C^{34}S$ $7-6$ line. [d] $[^{32}S]/[^{34}S]=22$ (Chin et al. 1996) was used. [e] From the H_2S $2_{2,0}-2_{1,1}$ line. [f] From the ^{34}SO 8_8-7_7 line. [g] From the SO_2 $22_{2,20}-22_{1,21}$ line. [h] From the SiO $8-7$ line. [i] From the H_2CO $3_{2,2}-2_{2,1}$ line. [j] From the HC_3N $25-24$ line. [k] From the $HCOOCH_3$ $20_{2,19}-19_{2,18}$ A line. [l] From the CH_3OCH_3 $21_{2,19}-20_{3,18}$ EE line. [m] From the rotational diagrams in Fig. 4.

4. DISCUSSION

MM1a and b of DR21(OH) appear to be a protobinary (or multiple) source consisting of typical hot cores, and new stars may be forming at these two cores separately. But MM1b shows stronger dust continuum emission than MM1a, and contains hypercompact HII regions (Araya et al. 2009). Methanol, which traces the very early stages of star formation, shows stronger emission towards MM1a than MM1b, suggesting that MM1b is slightly more evolved than MM1a. An interesting chemical difference was found between these two cores. Previously, small-scale spatial differences in the chemical composition have been observed toward many hot cores, which may have resulted from the different ice compositions, different ages, and/or the temperature effect (e.g., Viti & Williams 1999; Charnley et al. 2001; Rodgers & Charnley 2003). In this case, we expect that the same material is accreted to MM1a and MM1b, and hence there should be little difference in the ice compositions of these cores. The different temperatures, which can also result from the different ages, will lead to evaporation of different species at different epochs. Age difference will lead to different degrees of daughter molecule formations in the hot core gas phase. Hot cores are transient objects with a timescale of about 10^5 years since the new star is turned on (e.g., Viti & Williams 1999; Kurtz et al. 2000). During the early stage of the hot core phase, species evaporated from the heated grain mantles are expected to dominate the gas phase chemistry. But molecules will also be synthesized in the dense hot core gas phase mainly through the evaporated species, probably on a timescale of about 10^4 years (Rodgers & Charnley 2003; Nomura & Millar 2004). We think that MM1b has evolved a little further than MM1a, and their small age difference, probably on the order of 10^4 years, results in the chemical difference between these two hot subcores.

The different ages of these two cores is further characterized by, for instance, saturated species or sulfur-bearing species. CH_3OH is thought to evaporate directly from the ice grain mantles when the grains are heated up by various activities of newly formed stars, and this signifies a very early stage of the hot core evolution (e.g., Rodgers & Charnley 2003; van Dishoeck 2004). The fractional abundance of CH_3OH in MM1a is found to be more than 10 times smaller than in Orion Hot Core or W75N-MM1b although the fractional abundances of SO and SO_2 are pretty constant in these sources (Gibb et al. 2000; Minh et al. 2010). The main reason seems to be the less mass of MM1a, resulting in less energy to evaporate dust ice mantles, in addition to the possible interaction with MM1b which may destroy CH_3OH in MM1a. Highly saturated species, $HCOOCH_3$ or CH_3OCH_3, have been identified in MM1a together with CH_3OH with typical hot core abundances found in the galactic plane (e.g., Gibb et al. 2000). Chemical models suggest that the formation of $HCOOCH_3$ in the gas phase peaks at roughly 10^4 years after the injection of parent molecules, and is destroyed by ionic species with a timescale of $10^4 - 10^5$

years (Nomura & Millar 2004; Sakai et al. 2008). Sakai et al. (2008) argue that $HCOOCH_3$ should be produced over a shorter timescale in some protostars, and should evaporate from grain surfaces directly. Our results point at similar conclusions: namely, that MM1a is aged $\leq 10^4$ years, and these saturated species have not had enough time to be synthesized in the gas phase and are directly evaporating from ice mantles, together with CH_3OH. This early phase may also be signified by the H_2CS bipolar outflow associated with MM1a (Minh et al. 2011).

Highly saturated species are less abundant in the core of MM1b than in MM1a; this suggests that these species are being destroyed in MM1b. The sulfur-bearing species, such as SO or SO_2, become brighter in MM1b, and they probably exist in the turbulent gas with an elevated excitation temperature (e.g., Minh et al. 2010). These relatively simple sulfur-bearing species seem to have constant abundances throughout the hot core lifetime in the hot cores of W75N (Minh et al. 2010), although they quickly disappear after the hot core phase either by transforming to other species or by being accreted to the grain surface in the cold dense phase. It appears that the gas phase reactions between the evaporated sulfur- and oxygen-related species work efficiently through the hot core phase, but probably depend on the atomic carbon abundance (Gibb et al. 2000; Charnley et al. 2001; Van der Tak et al. 2003). We think that CS exists mainly in the envelope and did not include its fractional abundance in Table 4 since the H_2 column density is derived for the high temperature component in the hot core.

The H_2S abundance was found to be similar with those of W75N hot cores (Minh et al. 2010) but deficient by over an order magnitude compared to other hot cores in our galactic plane (Minh et al. 1991; Van der Tak et al. 2003). It is the only molecule among the observed species which does not peak toward either MM1a or b (the emission peaks at $\sim$ a few arcseconds south of MM1a). Therefore, H_2S may not be the major sulfur-bearing species in the ice mantles, at least in the hot subcores of DR21(OH). We found the SiO abundance to be similar to other dense star forming cores (Gibb et al. 2000; Martín-Pintado et al. 1992) where shocked turbulent gas may not have developed enough. HC_3N has a peak toward MM1b and probably an interacting region between MM1a and b, which suggests that this species may be forming in the high temperature turbulent gas.

5. CONCLUSIONS

Using the Submillimeter Array (SMA), we identified two bright hot subcores, MM1a and b (size $\sim 1''$ and mass ~ 0.5 $M_\odot$) separated by about $1.6''$ in the 230 GHz continuum emission toward the massive star-forming region DR21(OH). These two cores have typical hot core characteristics and have slightly different chemistries. The observed molecules show different emission distributions between these two hot subcores depending on the species. The highly saturated species, CH_3OH, $HCOOCH_3$ and CH_3OCH_3, show a stronger emission toward MM1a, while the emission from the sulfur-bearing species, SO and SO_2, peak toward MM1b where embedded sources and hypercompact HII regions have been found (Araya et al. 2009). We have suggested that the highly saturated species are being evaporated directly from the grain mantles together with CH_3OH. This occurs mainly at MM1a, as MM1a could be in an earlier stage than MM1b in the evolution of a massive star formation. Therefore, the small-scale chemical differences between these two cores may result from their small age difference probably of the order of 10^4 years.

ACKNOWLEDGMENTS

We are grateful to the staff of the SMA for their dedicated support in obtaining data.

REFERENCES

Araya, E. D., Kurtz, S., Hofner, P., & Linz, H. 2009, Radio Continuum and Methanol Observations of DR21(OH), ApJ, 698, 1321

Argon, A. L., Reid, M., J., &, Menten, K. M. 2000, Interstellar Hydroxyl Masers in the Galaxy. I. The VLA survey, ApJS, 129, 159

Batrla, W., & Menten, K. M. 1988, Detection of a Strong New Maser Line of Methanol toward DR 21(OH), ApJ, 329, L117

Charnley, S. B., Rodgers, S. D., & Ehrenfreund, P. 2001, Gas-Grain Chemical Models of Star-Forming Molecular Clouds as Constrained by ISO and SWAS Observations, A&A, 378, 1024

Chin, Y.-N., Henkel, C., Whiteoak, J. B., Langer, N., & Churchwell, E. B. 1996, Interstellar Sulfur Isotopes and Stellar Oxygen Burning, A&A, 305, 960

Fish, V. L., Muehlbrad, T. C., Pratap, P., Sjouwerman, L. O., et al. 2011, First Interferometric Images of the 36 GHz Methanol Masers in the DR21 Complex, ApJ, 729, 14

Genzel, R., & Downes, D. 1977, H_2O in the Galaxy: Sites of newly Formed OB Stars, A&AS, 30, 145

Gibb, E. L., Whittet, D. C. B., Schutte, W. A., et al. 2000, An Inventory of Interstellar Ices toward the Embedded Protostar W33A, ApJ, 536, 347

Hildebrand, R. H. 1983, The Determination of Cloud Masses and Dust Characteristics from Submillimetre Thermal Emission, QJRAS, 24, 267

Ho, P. T. P., Moran, J. M., & Lo, K. Y. 2004, The Submillimeter Array, ApJ, 616, L1

Kogan, L., & Slysh, V. 1998, VLA Imaging of Class I Methanol Masers at 7 Millimeters with Angular Resolution approximately 0.2 Arcseconds, ApJ, 497, 800

Kurtz, S., Cesaroni, R., Churchwell, E., Hofner, P., & Walmsley, M. 2000, Hot Molecular Cores and the Earliest Phases of High-Mass Star Formation, in Protostars and Planets IV, ed. V. Mannings, A. P. Boss, & S. S. Russell, 299 (Tucson: Univ. Arizona Press)

Kurtz, S., Hofner, P., & Álvarez, C. V. 2004, A Catalog of CH_3OH 7_0-6_1 A^+ Maser Sources in Massive Star-Forming Regions, ApJS, 155, 149

Lai, S.-P., Girart, J. M., & Crutcher, R. M. 2003, Interferometric Mapping of Magnetic Fields in Star-Forming Regions. III. Dust and CO Polarization in DR 21(OH), ApJ, 598, 392

Liechti, S., & Walmsley, C. M. 1997, Thermal Methanol Emission in the DR21 Complex. Interferometric Maps: A Comparison with Maser Emission, A&A, 321, 625

Lovas, F. J., Bass, J. E., Dragoset, R. A., & Olsen, K. J. 2009, in NIST Recommended Rest Frequencies (http://www.nist.gov/pml/data/micro/index.cfm)

Mangum, J. C., Wootten, A., & Mundy, L. G. 1991, Synthesis Imaging of the DR 21(OH) Cluster. I - Dust Continuum and C(O-18) Emission, ApJ, 378, 576

Martín-Pintado, J., Bachiller, R., & Fuente, A. 1992, SIO Emission as a Tracer of Shocked Gas in Molecular Outflows, A&A, 254, 315

Minh, Y. C., Ziurys, L. M., Irvine, W. M., & McGonagle, D. 1991, Abundances of Hydrogen Sulfide in Star-Forming Regions, ApJ, 366, 192

Minh, Y. C., Su, Y.-N., Chen, H.-R., Liu, S.-Y., Yan, C.-H., & Kim, S.-J. 2010, Submillimeter Array Observations toward the Massive Star-Forming Core of W75N, ApJ, 723, 1231

Minh, Y. C., Liu, S.-Y., Chen, H.-R., & Su, Y.-N. 2011, H_2CS Outflows of the Massive Star-Forming Core DR21(OH), ApJ, 737, L25

Motte, F., Bontemps, S., Schilke, P., Schneider, N., Menten, K. M., & Broguiére, D. 2007, The Earliest Phases of High-Mass Star Formation: A 3 Square Degree Millimeter Continuum Mapping of Cygnus X, A&A, 476, 1243

Nomura, H., & Millar, T. J. 2004, The Physical and Chemical Structure of Hot Molecular Cores, A&A, 414, 409

Norris, R. P., Booth, R. S., Diamond, P. J., & Porter, N. D. 1982, Interferometric Observations of Four Protostellar OH Maser Sources, MNRAS, 201, 191

Plambeck, R. L., & Menten, K. M. 1990, 95 GHz Methanol Masers near DR 21 and DR 21(OH), ApJ, 364, 555

Rodgers, S. D., & Charnley, S. B. 2003, Chemical Evolution in Protostellar Envelopes: Cocoon Chemistry, ApJ, 585, 355

Rygl, K. L. J., Brunthaler, A., Sanna, A., Menten, K. M., Reid, M. J., Van Langevelde, H. J., Honma, M., Torstensson, K. J. E., & Fujisawa, K. 2012, Parallaxes and Proper Motions of Interstellar Masers toward the Cygnus X Star-Forming Complex. I. Membership of the Cygnus X Region, A&A, 539, 79

Sakai, N., Sakai, K., & Yamamoto, S. 2008, Complex Organic Molecules in an Early Stage of Protostellar Evolution, Ap. Sp. Sci., 313, 153

Schneider, N., Bontemps, S., Simon, R., Jakob, H., Motte, F., Miller, M., Kramer, C., & Stutzki, J. 2006, A New View of the Cygnus X Region. KOSMA ^{13}CO 2 to 1, 3 to 2, and ^{12}CO 3 to 2 Imaging, A&A, 458, 855

Van der Tak, F. F. S., Boonman, A. M. S., Braakman, R., & van Dishoeck, E. F. 2003, Sulphur Chemistry in the Envelopes of Massive Young Stars, A&A, 412, 133

van Dishoeck, E. F. 2004, ISO SPECTROSCOPY OF GAS AND DUST: From Molecular Clouds to Protoplanetary Disks, ARA&A, 42, 119

Viti, S., & Williams, D. 1999, Time-Dependent Evaporation of Icy Mantles in Hot Cores, MNRAS, 305, 755

Woody, D. P., Scott, S. L., Scoville, N. Z., Mundy, L. G., Sargent, A. I., Padin, S., Tinney, C. G., & Wilson, C. D. 1989, Interferometric Observations of 1.4 Millimeter Continuum Sources, ApJ, 337, L41

Zapata, L. A., Loinard, L., Su, Y.-N., et al. 2012, Millimeter Multiplicity in DR21(OH): Outflows, Molecular Cores, and Envelopes, ApJ, 744, 86